JOURNAL OF SPACECRAFT AND ROCKETS
Vol. 41, No. 3, May–June 2004

Computational Evaluation of Quiet Tunnel Hypersonic Boundary-Layer Stability Experiments

Melissa L. Manning* and Ndaona Chokani†
North Carolina State University, Raleigh, North Carolina 27695

A computational assessment of two stability experiments conducted in the NASA Langley Research Center Nozzle Test Chamber equipped with the axisymmetric Mach 6 quiet nozzle is conducted. Navier–Stokes analysis of the mean flow and linear stability theory analysis of boundary-layer disturbances are performed. The computations show that adverse pressure gradient and wall cooling decrease the boundary-layer thickness and increase the frequency and amplification rate of the unstable second-mode disturbances; these findings are consistent with the experimental observations. The calculated surface pressure, wall temperature, and boundary-layer thickness distributions show very good overall agreement with experimental measurements. Comparisons between boundary-layer profiles derived from the calibrated hot-wire data and the mean flow computations show excellent agreement in the early stages of the transitional flow. However, examination of the wire Reynolds number and mass flux and total temperature eigenfunction profiles suggest that the mixed-mode sensitivity of the hot wire is complex. Thus, whereas uncalibrated hot-wire measurements are useful to characterize the qualitative features of the flow, calibrated hot-wire measurements are essential for quantitative comparison with stability theory.

Nomenclature

A, B	=	coefficients in equation for hot-wire time constant
a_w	=	overheat of hot wire
c_w	=	specific heat of hot wire
d	=	diameter of hot wire
e	=	voltage
$\boldsymbol{E}$, $\boldsymbol{F}$	=	flux vectors
E_0	=	total energy
f	=	frequency
i	=	$\sqrt{-1}$
J	=	Jacobian
k_a	=	thermal conductivity of air
M_w	=	hot-wire time constant
P, p	=	pressure
q	=	flow variable
Re	=	Reynolds number
R_w	=	resistance of hot wire
$\boldsymbol{S}$	=	source vector
$S_{\rho u}$, S_{To}	=	sensitivity coefficients
s	=	Laplace transform operator
T	=	temperature
T_c	=	hardware time constant of constant voltage anemometer
t	=	time
u	=	streamwise velocity
V_s	=	anemometer output voltage
v	=	streamwise normal velocity
w	=	spanwise velocity
x	=	distance along axis measured from model apex
y	=	surface normal distance measured from model surface
α	=	streamwise wave number
α_i	=	amplification rate
β	=	spanwise wave number
δ	=	boundary-layer thickness
ζ	=	spanwise transformed coordinate
η	=	surface normal transformed coordinate
ξ	=	streamwise transformed coordinate
ρ	=	density
ϕ	=	vector of disturbance variables
ω	=	disturbance frequency

Subscripts

e	=	boundary-layer edge
I	=	inviscid
rms	=	root mean square
V	=	viscous
w	=	wire
0	=	total or stagnation conditions
∞	=	conditions in the freestream

Superscripts

T	=	transpose of matrix
$'$	=	fluctuation
$\hat{}$	=	vector of conserved or flux variables
$\tilde{}$	=	eigenfunction
-	=	mean component

Received 26 September 2002; revision received 2 May 2003; accepted for publication 16 June 2003.

*Research Assistant, Department of Mechanical and Aerospace Engineering; currently Reentry Plasma Program Manager, U.S. Air Force Research Laboratory/VSBXT, Hanscom Air Force Base, MA 01731. Member AIAA.

†Professor, Department of Mechanical and Aerospace Engineering; currently Professor, Department of Mechanical Engineering and Materials Science, Duke University, Durham, NC 27708. Associate Fellow AIAA.

Introduction

THE location and extent of boundary-layer transition is a major issue in the design of hypersonic atmospheric and reentry vehicles. The nature of the boundary layer over the vehicle affects the aerodynamic performance of the vehicle, as well as the thermal protection and propulsion system requirements. In hypersonic flight, vehicles experience much higher skin friction and surface heat transfer due to transitional and turbulent boundary-layer flow than for laminar boundary-layer flow. Therefore, the delay of transition can result in significant drag reduction and can greatly reduce aerodynamic heating loads. For example, on a streamlined vehicle, the viscous drag can be 10% of the overall drag for fully laminar flow compared to 30% for fully turbulent.[1] Thus, there is a fundamental need for accurate laminar to turbulent boundary-layer transition prediction tools to improve vehicle design at hypersonic speeds.

Laminar to turbulent boundary-layer transition is a multistage process, which is initiated from an external disturbance field. This external disturbance field is internalized in the boundary layer, and then stages of linear and nonlinear growth of the internalized disturbances follow, before the onset of transition. In high-Mach-number boundary layers, the internalized disturbances are high-frequency, acoustical-type disturbances known as second-mode disturbances.[2,3] Acoustic disturbances are the primary source of the freestream disturbances in conventional high-speed wind tunnels. The acoustic disturbances, which radiate along Mach lines, emanate from convecting eddies in the turbulent boundary layer on the nozzle walls and are, thus, wind-tunnel specific. The disturbances interact with the boundary layer on the model and can contribute to early transition.[4,5] To obtain stability measurements that are indicative of free-flight conditions, wind tunnels with very low freestream disturbance environments, so-called quiet wind tunnels, are required. In a quiet wind tunnel, the freestream disturbance noise is brought to low levels by a number of design features, including wall suction just upstream of the throat and a well-designed nozzle expansion section.[6] As a result of the quiet wind-tunnel modifications, laminar boundary-layer flow is extended farther downstream on the nozzle walls, and low freestream acoustic disturbance levels are achieved in the test section. Since the early 1980s NASA Langley Research Center has pioneered the development of the quiet nozzle design. In the 1990s, a series of three pioneering hypersonic quiet-tunnel boundary-layer stability experiments were conducted; two of these experiments are studied in this work. Lachowicz and Chokani[7] detailed the growth of disturbances on a flared cone at 0-deg angle of attack. Blanchard and Selby[8] examined the effect of wall cooling on the evolution of disturbances into a nearly turbulent flow. When taken together, these experiments provided the first opportunity to examine the effects of adverse pressure gradient and wall cooling on boundary-layer stability in a hypersonic quiet tunnel.

Hot-wire anemometry is used to characterize the evolution of the pretransitional boundary-layer disturbances. Though the hot wire is intrusive, local spatial measurements of fluctuations in the flow can be readily obtained. A hot wire operated by a constant voltage anemometer[9] was used by Lachowicz and Chokani[7] and Blanchard and Selby.[8] In comparison to the more conventional constant current and constant temperature anemometers, only the constant voltage anemometer (CVA) provided the ability to obtain measurable signals in the electromagnetic interference environment of the Mach 6 quiet-tunnel facility. In a hypersonic flow, the hot wire operated by an anemometer responds to a mixed mode that has both mass flux and total temperature components:

$$e'/\bar{e} = S_{\rho u}[(\rho u)'/\bar{\rho}\bar{u}] + \boldsymbol{S}_{T_0}(T_0'/\bar{T}_0) \tag{1}$$

The sensitivity coefficients are commonly determined through a hot-wire calibration.[10] However, Lachowicz et al.[11] observed that the CVA-operated hot wire is more sensitive to mass flux when the hot wire is operated in high-overheat mode and more sensitive to total temperature when the hot wire is operated in low-overheat mode. This feature was exploited by Blanchard and Selby[8] and Lachowicz and Chokani,[7] who primarily obtained uncalibrated high-overheat mode hot-wire measurements of the boundary-layer fluctuations. However, in the study by Lachowicz and Chokani,[7] a calibration was performed for one of the hot wires, and boundary-layer measurements were obtained using this hot wire. The objective of this paper is to assess the overall quality of the experimental measurements, in particular the CVA-operated hot-wire measurements, obtained in the quiet-tunnel experiments. This assessment is of value in the development of future quiet wind-tunnel hypersonic stability experiments.

Quiet Wind-Tunnel Experiments

The two boundary-layer stability experiments examined in this work were conducted in the NASA Langley Research Center's Nozzle Test Chamber Facility installed with the Mach 6 axisymmetric quiet nozzle. This is an open-jet blowdown facility. A tunnel stagnation temperature of $810 \pm 3°$R (450 ± 1.7 K), a total pressure of 130 ± 2 psia (896.3 ± 13.8 kPa), and a freestream Mach number of 5.91 ± 0.08 are used. These conditions correspond to a unit Reynolds number of 2.82×10^6/ft (9.25×10^6/m).

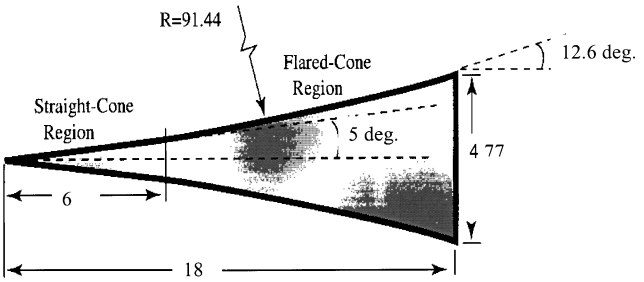

Fig. 1 Cone-flare 91–6 model and dimensions, from Ref. 8; dimensions in inches.

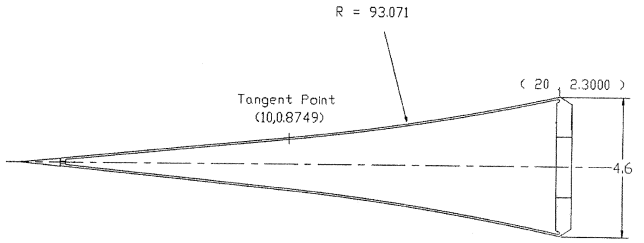

Fig. 2 Cone-flare 93–10 model and dimensions, from Ref. 7; dimensions in inches.

Two flared-cone configurations are examined in this work. Both models have a straight, 5-deg. half-angle section that tangentially merges into a flared region. The tangent circular arc flare produces a nearly linear adverse pressure gradient.[12] The effect of the adverse pressure gradient and wall cooling on the onset of transition for the two flared-cone configurations, as determined from the N factor, is presented in Ref. 12. Wilkinson[12] also presents a comparison of the computationally inferred N factors and the N factors derived from experiment; this comparison shows that transition onset is observed on the models. Without the pressure gradient, transition could not have been attained within the limited quiet flow Reynolds number range of the facility (see Ref. 13).

The model used by Blanchard and Selby[8] consists of a 6-in. (15.25-cm) straight portion followed by a 12-in. (30.5-cm) outward flared region with a 91.44-in. (232.2-cm) radius of curvature (Fig. 1). This configuration is denoted 91–6 referring to the approximate radius of the circular flare arc and the location of the tangency point, respectively. The cone is thin walled and is equipped with internal passages for active surface cooling; the cone tip is not cooled. Nominally adiabatic-wall and cooled-wall (465°R; 258 K)-temperature conditions are examined for the 91–6 model. The thin-walled cone model used by Lachowicz and Chokani,[7] configuration 93–10, consists of a 10-in. (25.4-cm) straight portion followed by a 10-in. flared region with a 93.07-in. (236.4-cm) radius of curvature (Fig. 2). This cone-flare configuration results in a smaller adverse pressure gradient applied over a smaller extent of the model than for the 91–6 model. Only adiabatic-wall conditions are examined for the 93–10 model. Hot-wire measurements were obtained at 31 streamwise stations over the range $9.0 \le x \le 16.5$ in. ($22.9 \le x \le 41.9$ cm) on the 91–6 model. For the 93–10 model, hot-wire measurements were obtained over the range $11.0 \le x \le 19.0$ in. ($27.9 \le x \le 48.3$ cm).

Computational Methods

The computational procedure for this work consists of two parts: calculation of a mean flow solution and linear stability analysis. Smooth profiles of the first and second derivatives of velocity and temperature must be obtained on a well-resolved grid for linear stability analysis to capture instabilities accurately in the flow.[14] A standard transfinite interpolation algebraic method is used to generate the grid. In the streamwise direction, grid points are spaced equally between the model tip and base. A one-sided, geometric progression spacing algorithm is used to distribute points in the surface-normal

Table 1 Description of cases for grid refinement study on 91–6 model

Case	Number of points in boundary layer	Grid dimensions	Grid spacing $x = 0$ in.		Grid spacing $x = 18$ in.	
			$\eta_{\min} \times 10^{-6}$	$\eta_{\max} \times 10^{-4}$	$\eta_{\min} \times 10^{-5}$	$\eta_{\max} \times 10^{-3}$
1	40	241×145	9.93	9.80	9.60	9.70
2	45	241×225	9.99	2.10	8.80	1.29
3	90	241×225	9.89	2.10	0.90	2.48
4	105	241×225	9.77	2.12	0.90	5.39

direction, and the minimum wall spacing is specified. The number of points located within the boundary layer is also specified. A grid refinement study was conducted to evaluate the smoothness of the velocity and temperature derivatives with respect to the overall grid dimensions and grid clustering within the boundary layer. Table 1 summarizes the description of the grids that were used in the grid refinement study conducted on the 91–6 cone. Once the optimal grid was determined for the 91–6 cone, similar grid dimensions and spacings were used for the 93–10 cone. More complete details are presented in Ref. 15. The mean flow solution was then postprocessed and used in the linear stability analysis.

Mean Flow Analysis

The mean flow analysis is conducted using a Navier–Stokes code written by Edwards.[16–18] The governing equations of the mean flow are the axisymmetric compressible Navier–Stokes equations. These equations, written in strong conservation-law form using curvilinear, axisymmetric coordinates, are given by

$$\frac{\partial \hat{\boldsymbol{U}}}{\partial t} + \frac{\partial(\hat{\boldsymbol{E}}_I - \hat{\boldsymbol{E}}_V)}{\partial \xi} + \frac{\partial(\hat{\boldsymbol{F}}_I - \hat{\boldsymbol{F}}_V)}{\partial \eta} = \hat{\boldsymbol{S}} \tag{2}$$

The vector of conserved variables is given by

$$\hat{\boldsymbol{U}} = (y/J)(\rho, \rho u, \rho v, E_0)^T \tag{3}$$

The equations are marched in time, using a nonlinear line Gauss–Seidel approach (see Ref. 16). An implicit full-multigrid/full-approximation-storage technique is used to accelerate the convergence to a steady state.[17] The inviscid components of the Navier–Stokes equation set are discretized using an upwind scheme. A high-resolution, low-diffusion, flux-splitting approach, which combines the accuracy of flux-difference splitting in the capturing of shear layers with the robustness of flux-vector splitting, is employed.[18] In this approach, the inviscid flux at a cell interface is split into a convective contribution, which is upwinded in the direction of the flow, and a pressure contribution, which is upwinded based on acoustic considerations. The monotone capturing of strong oblique shock waves that are not aligned with a mesh line is accomplished by constraining the cell interfaces to behave as a stationary contact discontinuity for vanishing numerical diffusion. The upwind scheme is second-order accurate. The viscous components of the Navier–Stokes equations are central differenced to second-order accuracy.

At the cone wall, no-slip boundary conditions are applied; in addition, either adiabatic- or isothermal-wall conditions are applied. At the top boundary, freestream conditions are imposed, and a zero-gradient condition is imposed on all variables. Freestream supersonic conditions are applied at the inflow, and first-order supersonic characteristic boundary conditions are imposed at the outflow. The run time is less than 5 min of CPU on a Cray T-90.

Linear Stability Analysis

Linear stability analysis is performed using the quasi-parallel, spatial stability theory code written by Hudson et al.[19] The code was developed for stability analysis in two and three dimensions of perfect and thermochemical nonequilibrium gas flows; first- and second-mode disturbances may be modeled. For the present work, second-mode disturbances in perfect gas flow are analyzed. To formulate the linear stability equations, each flow variable is first separated into a mean and fluctuating component. These equations are substituted into the governing equations (2), and the resulting equations are linearized. Linearity assumes that there are no interactions between the disturbances and, thus, only the second-mode disturbance is predicted. The mean flow is then subtracted from the linearized equations. A quasi-parallel flow assumption is imposed such that the mean flow quantities at a given location depend only on the surface-normal distance from the wall. The fluctuating quantities are assumed to be small amplitude harmonic waveforms of the form

$$q'(\xi, \eta, \zeta, t) = \tilde{q}(\eta) \exp[\iota(\alpha\xi + \beta\zeta - \omega t)] \tag{4}$$

The spatial growth of a two-dimensional disturbance is examined such that the frequency is real, the streamwise wave number is complex, and the spanwise wave number is nonzero. When Eq. (4) is substituted into Eq. (2) for the fluctuating quantities, it can be shown that the linear disturbances satisfy the following system of ordinary differential equations:

$$\left(A\frac{\mathrm{d}^2}{\mathrm{d}y^2} + B\frac{\mathrm{d}}{\mathrm{d}y} + C\right)\phi = 0 \tag{5}$$

where A, B, and C are 5×5 matrices whose nonzero elements are given by Malik[20] and

$$\phi = (u', v', p', T', w')^T \tag{6}$$

A no-slip wall boundary condition is assumed such that the velocity fluctuations are zero at the cone surface. The temperature fluctuations are also assumed to be zero at the wall due to the thermal inertia of the cone. All velocity disturbances, except in the y direction, and temperature disturbances are assumed to be zero in the freestream.[20] Thus, the boundary conditions are

$$u' = v' = T' = w' = 0 \qquad \text{at} \qquad y = 0$$
$$u' = T' = w' = 0 \qquad \text{at} \qquad y = \infty \tag{7}$$

The pressure is calculated using the momentum equation.

The numerical methods used to solve the eigenvalue problem employ global and local methods, depending on the availability of an initial eigenvalue guess.[21] When no guess is available, the global approach is employed wherein a spectrum of eigenvalues of the discretized differential equation is obtained and then filtered to determine the most unstable eigenvalue. The local approach is then employed to improve on the approximate eigenvalue obtained from the global method. Standard matrix eigenvalue problem algorithms are employed for the global methods, whereas iterative solution algorithms are used for the local method. The run time for a global and local solution for one frequency is less than 2 min of CPU on a Cray T-90.

Results and Discussion

The effects of wall cooling are examined from the adiabatic- and cooled-wall conditions on the 91–6 model. The effects of adverse pressure gradient are examined by comparing the 91–6 and 93–10 models under adiabatic-wall conditions. In the following, the results of the grid refinement study are first presented. Next, the pressure gradient and wall-cooling effects are first examined in terms of the computed mean flow profiles of velocity, mass flux, and total temperature. Then, the mean flow profiles are compared with available experimental data. Next, amplification rate calculations from

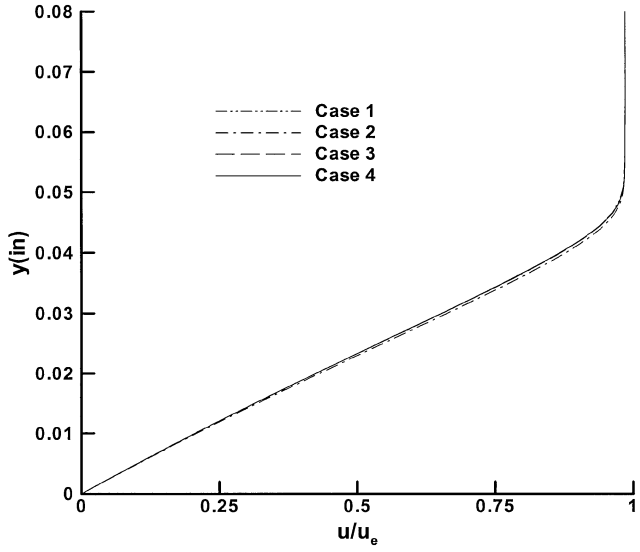

Fig. 3a Effect of grid spacing on velocity profiles; $x = 9$ in.

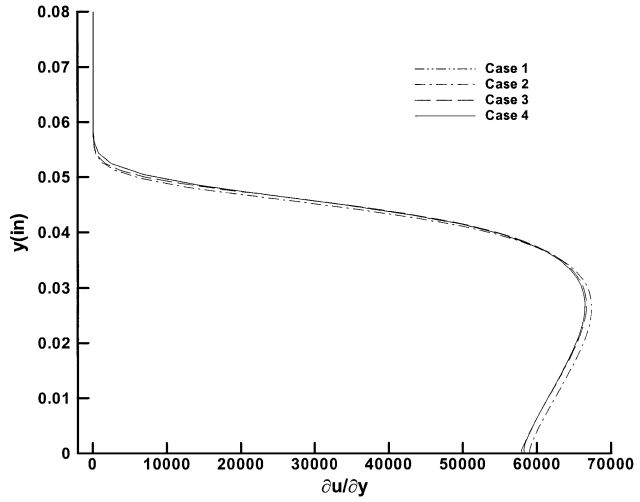

Fig. 3b Effect of grid spacing on first derivative of velocity profiles; $x = 9$ in.

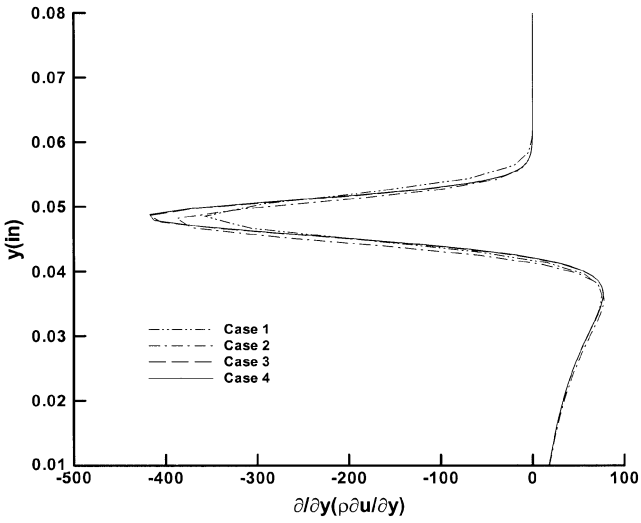

Fig. 3c Effect of grid spacing on generalized inflection point profiles; $x = 9$ in.

linear stability theory (LST) are presented to examine the effects of pressure gradient and wall cooling on the boundary-layer stability. The response of the uncalibrated hot wire to boundary-layer fluctuations are examined. Recommendations for future quiet-tunnel experiments are also presented.

It is essential to have smoothness in the profiles of the first and second derivatives of the mean flow variables to ensure accuracy in the linear stability results.[14] The profiles of the velocity, first derivative of velocity, and the generalized inflection point for the four cases examined in the 91–6 grid refinement study are presented in Fig. 3. Figure 3 confirms the smoothness of the profiles and also shows that the mean flow solutions on the two finest grids (cases 3 and 4) are grid independent; the results to be presented use case 4, which has 241×225 points in the streamwise and surface-normal directions. Similar dimensions were chosen for the 93–10 model (Table 2).

The hot wire is sensitive to mass flux and total temperature fluctuations, and the sensitivity coefficients of the hot wire are a function of the mean flow. Thus, the hot-wire calibration, that is, the determination of the sensitivity coefficients, must account for the mean total temperature and mean mass flux range within the measurement region. The value of the mean mass flux profile for the 91–6 model varies from 0 to 1.7 times the freestream value over the height of the boundary layer, as seen in Fig. 4; the variation for the 93–10 model is slightly smaller. The total temperature profiles for the 91–6 and 93–10 models are shown in Fig. 5. The total temperature variation through the boundary layer is much larger for the cooled-wall case than for the adiabatic-wall cases. Figures 4 and 5 shows that the hot-wire calibration for measurements through the boundary layer must cover a wide range of mass flux and total temperature. Also, for the case of the cooled wall, the hot wire must be calibrated over a wider range of total temperature than for the adiabatic wall. Furthermore, for both the adiabatic- and cooled-wall cases, the overshoot in total temperature at the boundary-layer edge necessitates hot-wire calibration at temperatures in excess of the freestream total temperature value. This wide range of parameters can most efficiently and economically be obtained by performing the hot-wire

Table 2 Grid spacing for 93–10 model

Parameter	Value
Number of points in boundary layer	85
Grid dimensions	241×225
Grid spacing $x = 0$ in.	
$\eta_{\min} \times 10^{-7}$	9.91
$\eta_{\max} \times 10^{-4}$	3.88
Grid spacing $x = 20$ in.	
$\eta_{\min} \times 10^{-5}$	4.90
$\eta_{\max} \times 10^{-3}$	4.53

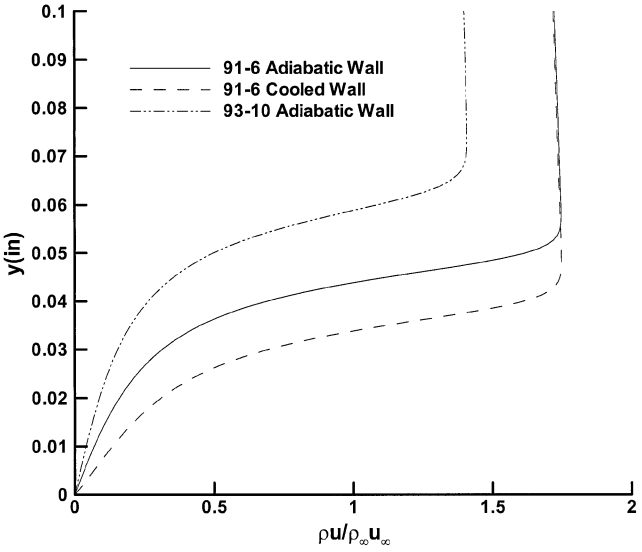

Fig. 4 Mass flux profiles at $x = 11$ in.

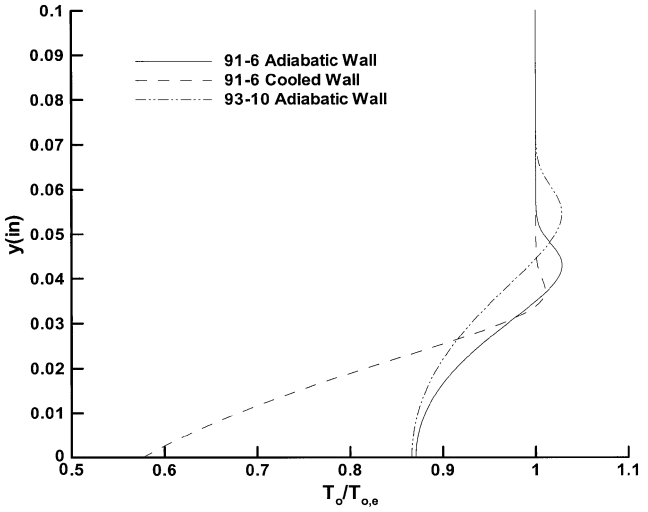

Fig. 5 Total temperature profiles at $x = 11$ in.

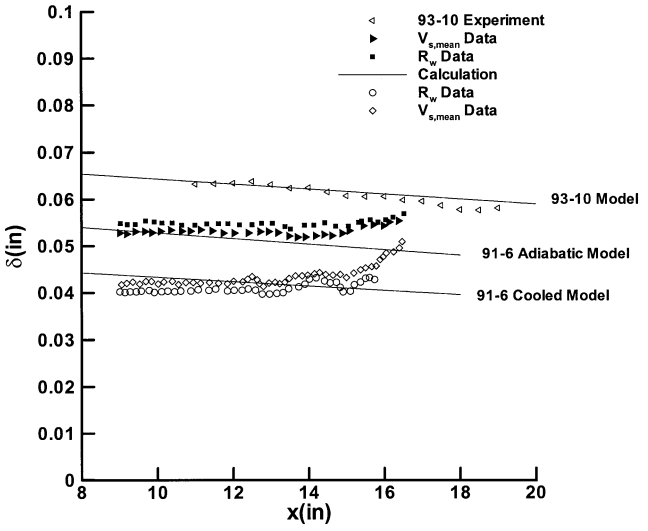

Fig. 6 Boundary-layer thickness distribution.

calibration in a small (nozzle exit diameter 1.5–2.0 in.) calibration tunnel rather than in the relatively large (nozzle exit diameter 7.9 in.) Mach 6 axisymmetric quiet nozzle. Specifically, although their range of operations may be the same, the mass flow requirement of the small-calibration tunnel compared to the Mach 6 quiet nozzle is reduced by the ratio of the square of the diameters; additionally, the heating requirements for control of total temperature are less.

Figure 6 shows a comparison of the predicted and experimentally determined boundary-layer thickness distributions. In the 91–6 experiment the boundary-layer thickness was determined using two methods.[7] In the first method, denoted R_w data, the boundary-layer thickness is determined as the value of y, where the resistance of the hot wire, operated in its low-overheat mode, is the same as the resistance at the outer edge. In the second method, the $V_{s,\text{mean}}$ data, the boundary-layer thickness is the value of y where the mean voltage of the hot wire, operated in its high-overheat mode, is 99% of its value at the boundary-layer edge. In the calculations, the boundary-layer thickness is specified as the location where the vorticity is less than 0.04% of the maximum vorticity; this value is then bounded by the criterion that the local velocity is 99.5% of the freestream velocity.[14] Overall, the computed boundary-layer thickness results for the 91–6 adiabatic model show slightly better agreement with experimental results than the 91–6 cooled-model calculations. For the adiabatic model, it is seen that upstream of $x = 15$ in. the predicted boundary-layer thickness and the experimental measurements agree within 3%. Chokani[22,23] has shown that at $x = 12$ in. nonlinear effects begin to become important and by $x = 13$ in. dominate the interactions in the boundary layer for the 91–6 model. Downstream of $x = 15$ in. for the adiabatic model, different trends are indicated by the experiment and computation; for the cooled model, this difference is first observed at $x = 13$ in. The difference in trends downstream of $x = 15$ in. (adiabatic model) and $x = 13$ in. (cooled model) are thought to occur because the computed flow is wholly laminar, whereas in the experiment the flow is transitional. A comparison between measured and computed boundary-layer thickness distributions for the 93–10 model is also shown. Because of the more adverse pressure gradient, the 91–6 model has a thinner boundary-layer than the 93–10 model. In the experiment, the boundary-layer thickness on the 93–10 model was determined as the location where the output voltage of the CVA, operated in low-overheat mode, is 99.5% of the value farthest from the wall.[8] Upstream of $x = 15$ in., the agreement between the experimental measurements and the calculation is within 1%. Downstream of $x = 15$ in., the computed flow is laminar, whereas the actual flow is now transitional and a larger difference is seen. In summary, the boundary-layer thickness determined experimentally using three different criteria are compared with one criterion from the computations. The experimental criterion that is based on the anemometer output voltage, in low-overheat mode, shows the best agreement with the computations.

Figure 7 shows a comparison of the wall static pressure. The 91–6 calculations agree very well with the experimental data. The small differences between the experiment and calculation possibly arise from model misalignment. The pressure distributions for the 93–10 adiabatic model are also shown in Fig. 7. Good agreement is seen between the experiment and calculation and the difference is within 6%. Overall there are only small differences between the experiment and computation. However, Doggett et al.,[24] using the 93–10 model, have shown that even small angles of attack can have a marked effect on the boundary-layer stability. In future experiments, it may be useful to conduct pressure measurements along a 180-deg out-of-phase ray, preferably within a single tunnel run, to assess the possible effects of model misalignment.

The computed and experimentally measured temperature distributions for the 93–10 and 91–6 models are shown in Fig. 8. Lachowicz and Chokani[7] qualitatively observed that nonlinear interactions of the boundary-layer disturbances are first observed at $x = 15$ in. for the 93–10 model. Upstream of $x = 15$ in., the computational and experimental results agree within 1%. The rise in temperature occurs farther downstream on the 93–10 model compared to the 91–6 model ($x = 12$ in.) due to the smaller adverse pressure gradient on the 93–10 model. The rise in the measured temperature at $x = 12$ in. for the 91–6 adiabatic model is due to the transitional nature of the boundary layer. Upstream of this location, the predictions and experiment are in very good agreement, within

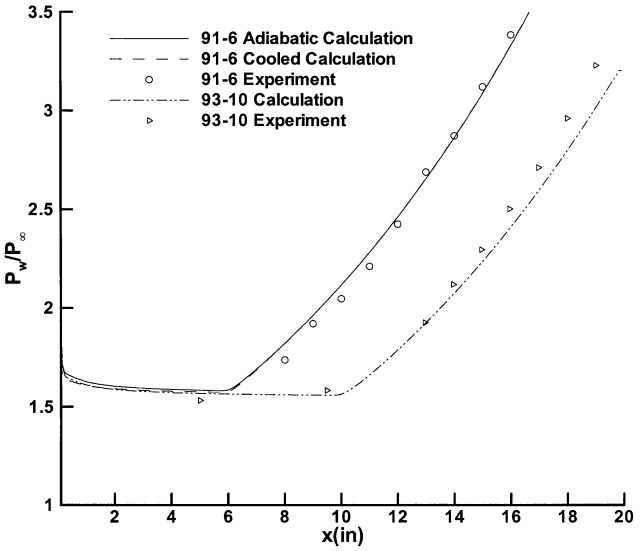

Fig. 7 Surface pressure distribution.

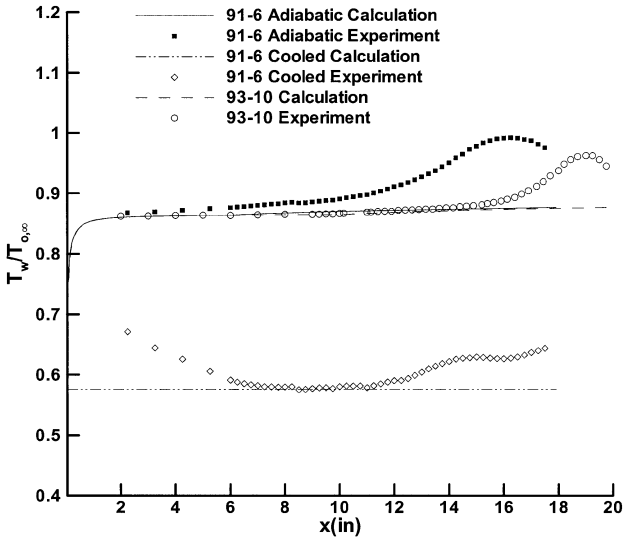

Fig. 8 Temperature distribution.

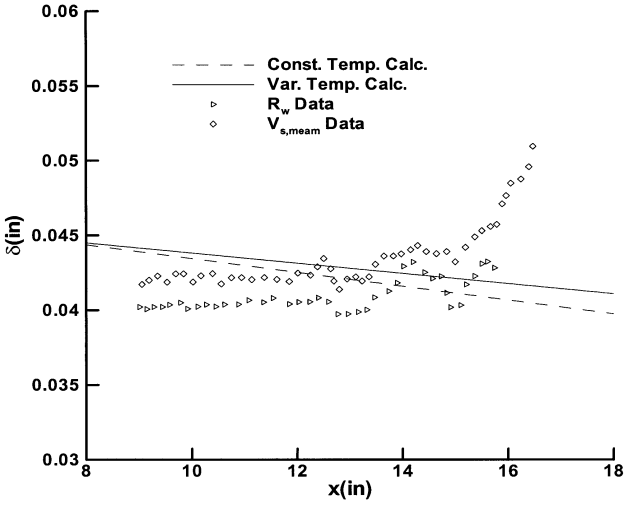

Fig. 9 Effect of wall temperature on boundary-layer thickness; 91–6 model.

3% of each other. A discrepancy between the experiment and computations on the cooled model is observed upstream of $x = 6$ in. The computational results are obtained for a constant wall temperature. However, the tip of the thin-walled cone model is not cooled. Therefore, a temperature gradient exists between the relatively hot tip and the cooler thin wall downstream of the leading-edge region. A uniform wall temperature is not achieved until $x = 7$ in. In the range of $7 \leq x \leq 12$ in., the calculated and measured results agree to within 1%. The differences between the experimental and computational results downstream of $x = 12$ in. are due to the onset of transition. In addition to the transitional nature of the boundary layer in the experiment, there are other possible sources for the differences between experiment and computation. In the experiment, a preheat procedure is used to bring the nozzle and model into thermal equilibrium. Following preheat, the hypersonic flow is started, and the measurements are subsequently taken. If adiabatic-wall conditions are not achieved, this may be a source of some discrepancy. However the careful attention to this preheat procedure minimized the likelihood that this is a source of error.[7] A second possible source of error is that the cone tip is solid, whereas the cone wall is thin. Thus, for the case of the adiabatic wall, where the wall normal temperature gradient may be negligible (ideally zero), the wall parallel temperature gradient may be significant and the heat conduction along the thin-skin wall may be the source of some differences. The sensitivity of the mean flow solution for the 91–6 cooled model to the wall temperature boundary condition is examined in Fig. 9. A curve fit

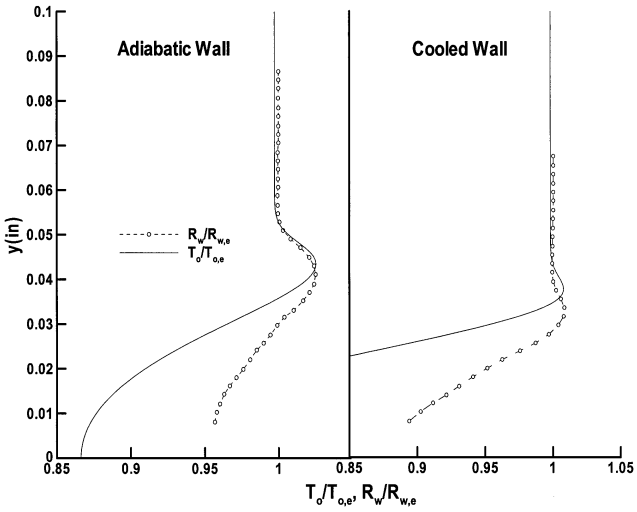

Fig. 10 Total temperature and normalized wire resistance; 91–6 model.

to the experimentally measured wall temperature is used as the wall boundary condition for the mean flow calculation. The distribution of the calculated and measured boundary-layer thickness, shown in Fig. 9 over the range of the experimental measurements, agree to within 2% in the linear growth region (upstream of $x = 13$ in.); thus, very little effect of the wall temperature distribution is seen. The increased wall temperature upstream of $x = 6$ in. has little effect on the mean flow profiles as well.[15] Thus, it appears that the constant wall temperature distribution is suitable for modeling the mean flow over the 91–6 cooled model.

Blanchard and Selby's[8] hot-wire measurements were uncalibrated, and thus, no direct comparisons can be made between mean flow computations and experimental measurements. Lachowicz et al.[11] observed that the CVA, as with the constant current and constant temperature anemometers, is more sensitive to mass flux when the hot wire is operated in high-overheat mode and more sensitive to total temperature when the hot wire is operated in low-overheat mode. Figure 10 shows a comparison of the normalized mean total temperature and the normalized hot-wire resistance obtained in low-overheat mode at $x = 9$ in. for the 91–6 model with adiabatic- and cooled-wall conditions. In both cases the measured data show the overshoot at the boundary-layer edge that is also observed in the computed total temperature profiles. The magnitudes of the overshoot are also in good agreement. However, within the boundary layer, the difference between the experiment and computation is increasingly larger. One possible reason for the difference is that the uncalibrated hot wire, although operated in low-overheat mode, has a constant wire voltage and not a constant overheat.[25] Therefore, the hot wire has different sensitivities to the total temperature and mass flux, as the wall is approached. Thus, the quantitative trends across the boundary layer of the uncalibrated hot-wire measurements, in low-overheat mode, may not reliably be compared with the computed mean total temperature profiles. This serves to emphasize the need to obtain calibrated hot-wire measurements in future experiments.

In Lachowicz and Chokani's[7] experiment, a calibration was performed for one of the hot wires. The hot wire was calibrated by determining the hot-wire sensitivities for a given wire voltage in a series of known freestream flows. This procedure was repeated for different wire voltages. Then, boundary-layer measurements were conducted with the hot wire operated at different wire voltages at each measurement point to determine the mass flux and total temperature. The experimentally determined mass flux and total temperature profiles using the calibrated hot wire are compared with calculations in Figs. 11 and 12 for the 93–10 model. At $x = 13.5$ in., where the flow is laminar, the agreement between experiment and computation is very good. Lachowicz and Chokani[7] observed that nonlinear interactions are significant in the flow downstream of $x = 15$ in. Therefore, at the more downstream locations, only fair agreement

is observed between the experiment and computation. These differences are attributed to the transitional character of the boundary-layer flow.

The large bandwidth (range of frequencies) is one of the primary reasons for employing hot-wire anemometry in hypersonic stability experiments. The bandwidth of the CVA is superior to that of the constant current and constant temperature anemometers. However, the time constant of the CVA-operated hot wire is a function of the Reynolds number (see Ref. 26):

$$M_w^{=} \frac{1+a_w}{1+2a_w} \frac{d^2 \rho_w c_w}{4k_a} \frac{1}{A+B\sqrt{Re_w}} \tag{8}$$

Furthermore, as shown by Sarma[9] the output voltage of the CVA in response to a fluctuation in the fluid flow is proportional to a ratio of the hardware time constant and hot-wire time constant:

$$\frac{e'(s)}{u'(s)} \propto \frac{1+sT_c}{1+sM_w} \tag{9}$$

Therefore, it is of interest to assess the effect of the wire Reynolds numbers on the fluctuating hot-wire measurements because a fixed hardware time constant was used in the experiments of Blanchard and Selby[8] and Lachowicz and Chokani.[7] This approach of a fixed hardware time constant enhances the productivity using the CVA.[27] However, it may be necessary to compensate for the mismatched hardware and hot-wire time constants if it is desired to infer quantitative information of the disturbances growth or profiles of disturbance eigenfunctions. For the 2.5-μm (0.0001-in.)-diam hot wire used in the experiments, the profiles of the calculated wire Reynolds number across the boundary layer are shown for various streamwise locations in Fig. 13. The filled circles denote the boundary-layer thickness at each streamwise location. The hot-wire measurements that are used to derive the growth rates are obtained in the outer portion of the boundary layer, 0.9δ–1.0δ, because it is within this range that the rms disturbance energy is observed to be a maximum.[7,8] In Fig. 13, the wire Reynolds number varies over the range 7–20 for the 91–6 model and 19–30 for the 93–10 model at the boundary-layer edge. The hot-wire time constant, thus, varies little for measurements conducted at the boundary-layer edge on the 93–10 model, but substantially for the 91–6 model. Therefore, the hot-wire measurements at the boundary-layer edge for the 93–10 model over the measurement range of $11.0 \le x \le 19.0$ in., even without software compensation, are a good quantitative indicator of the disturbance growth; this is, however, not the case for the 91–6 model over its measurement range of $9.0 \le x \le 16.5$ in. On both models, over the height of the boundary layer, the large variation of the wire Reynolds number, 0–30, indicates that software compensation of the hot-wire measurements for the mismatched hardware and hot-wire time constants is necessary if eigenfunction profiles are to be derived.

The amplification rates for the 91–6 adiabatic and cooled models and 93–10 adiabatic model at $x = 14$, 15, and 16 in. are plotted in Fig. 14. These results are obtained by determining the range of unstable frequencies at each streamwise location. The results show three expected trends. First, for each test case the amplification rates increase with increasing streamwise distance. Second, the effect of adverse pressure gradient and wall cooling is destabilizing. Third, the

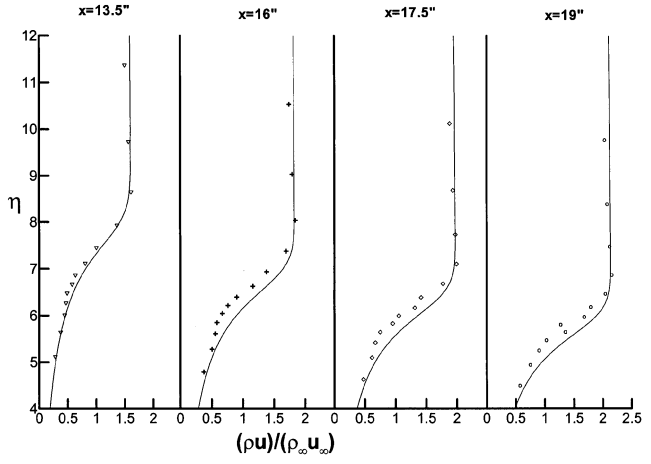

Fig. 11 Mass flux profiles, 93–10 adiabatic model: ——, computational data and ▽, +, ◇, and ○, experimental data.

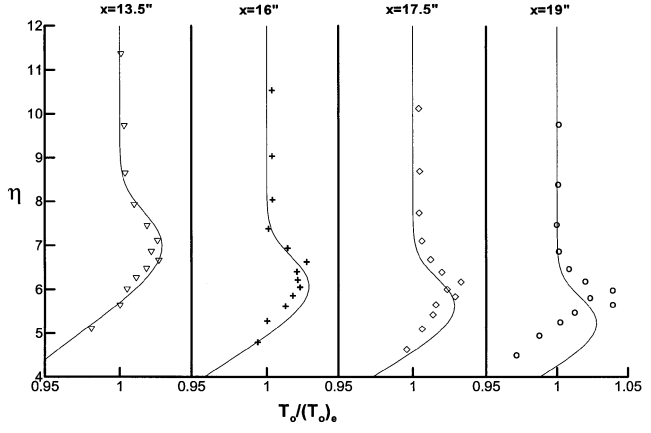

Fig. 12 Total temperature profiles, 93–10 adiabatic model: ——, calculated data and ▽, +, ◇, and ○, experimental data.

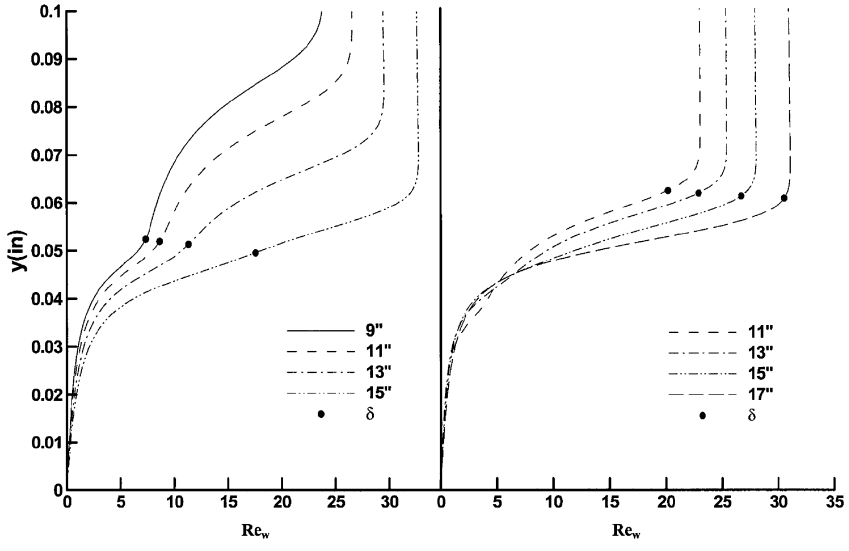

Fig. 13 Wire Reynolds number: a) 91–6 adiabatic model and b) 93–10 adiabatic model.

Table 3 Measured and predicted unstable frequency bands and frequency of most unstable second mode

	LST, kHz		Experiment, kHz	
Model	Unstable band	Peak	Unstable band	Peak
93–10	160–240	190	170–275	230
91–6 Adiabatic	190–285	230	225–345	275
91–6 Cooled	220–310	260	235–385	306

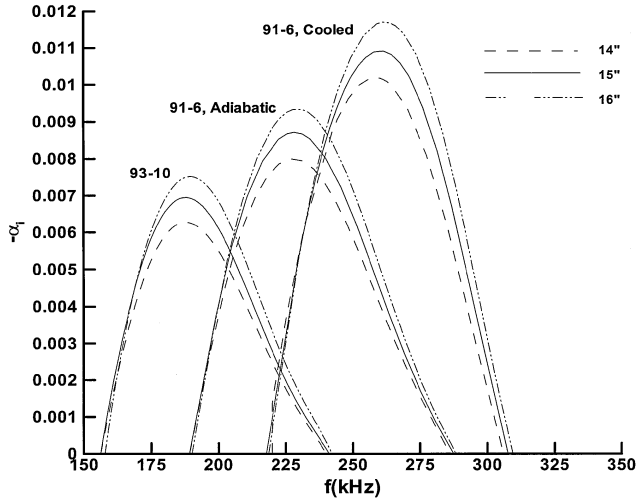

Fig. 14 Amplification rates for 91–6 and 93–10 models.

range of unstable frequencies increases as the boundary-layer thickness decreases; thus, the 93–10 model has a relatively low-frequency band of unstable disturbances, whereas the 91–6 cooled model has a relatively high-frequency band. This tuning of the most amplified second-mode disturbances has been experimentally observed by Stetson et al.,[28] Lachowicz and Chokani,[7] and Kimmel et al.,[29] among others, and was first suggested in the LST analysis of Mack.[2] For the 93–10 model, the range of unstable frequencies lie in a band between 160 and 240 kHz, which is centered on a most unstable frequency of 190 kHz. Lachowicz and Chokani[7] measured an unstable frequency band of 170–275 kHz, centered on 230 kHz. For the 91–6 adiabatic model, LST predicts an unstable band of 190–285 kHz centered on 230 kHz, and in the experiment, Blanchard and Selby[8] observe a peak frequency of 275 kHz in a band of 225–345 kHz. On the 91–6 cooled model, an unstable frequency band of 235–385 kHz centered on a frequency of 306 kHz is measured; a peak frequency of 260 kHz in an unstable band of 220–310 kHz is predicted by LST. These results are summarized in Table 3. Doggett et al.[24] used the results of three-dimensional Navier–Stokes computations to examine the effect of small-angle variations of the most amplified disturbance frequency on the 93–10 model. The frequency of the most amplified disturbance at $x = 13$ in. changed by 55 kHz with 0.2-deg change in angle of attack. This observation and the present LST predictions suggest that, whereas in the experiments of Blanchard and Selby[8] and Lachowicz and Chokani[7] the hot-wire measurements were conducted along one streamwise plane, in future experiments, it may also be useful to conduct measurements along the 180-deg out-of-phase streamwise plane to resolve uncertainties with regards to the most unstable band of frequencies. Note that in linear stability theory, there is an inherent assumption that the disturbances of different frequencies do not interact, and this may also be a source of some discrepancy. Another source of error may be the parallel flow assumption in the LST approach. If initial disturbance levels from calibrated hot-wire measurements were available, it would be useful to use the parabolized stability equation approach to examine nonlinear and nonparallel flow effects. Therefore, calibrated hot-wire measurements are strongly recommended for future experiments.

In Fig. 9, the effect of wall temperature distribution on the mean flow was examined. The effect of the wall temperature distribution on the boundary-layer stability is shown in Fig. 15. It is seen that

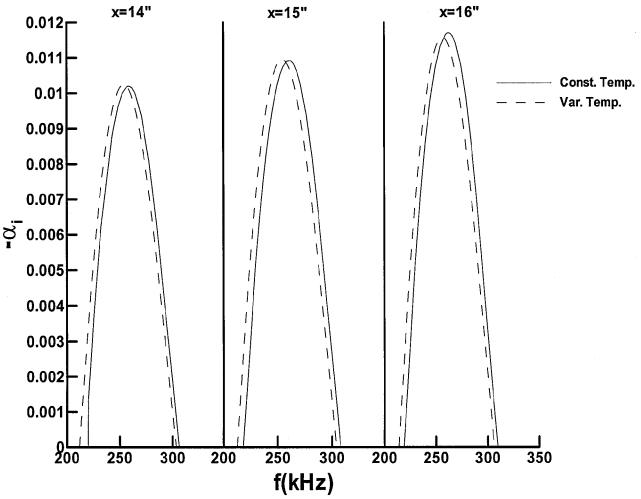

Fig. 15 Effect of wall temperature distribution on amplification rates.

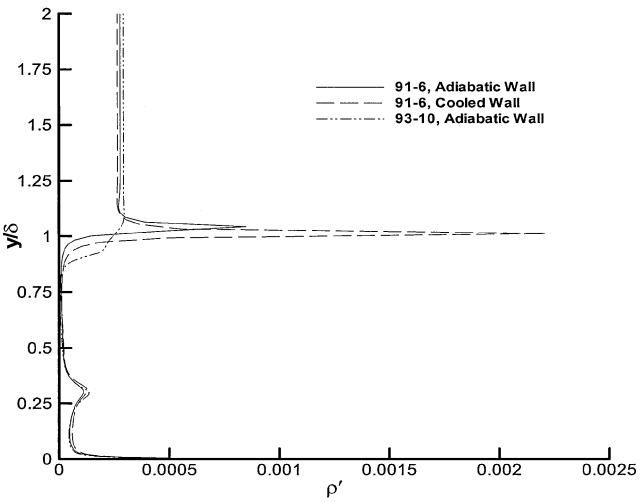

Fig. 16 Density eigenfunction for 91–6 and 93–10 models at $x = 13$ in.

the temperature distribution has very little effect on the magnitude of the amplification rates and, thus, on the boundary-layer stability. Kimmel and Poggie[30] conducted experimental measurements on a cone at Mach 6 and observed that the presence of a hot nose tip on the model has little effect on the boundary-layer stability or transition data. The boundary layer is 5% thicker for the variable wall temperature calculation (Fig. 8), and thus, the range of unstable frequencies for the variable wall temperature distribution are 5-kHz smaller than for the constant wall temperature distribution.

The eigenfunctions of the density of the most amplified disturbances for the 93–10 and 91–6 models at $x = 13$ in. are shown in Fig. 16. Two peaks in the density eigenfunction are seen at approximately 30% of boundary-layer thickness and at the boundary-layer edge. The velocity eigenfunctions are shown in Fig. 17. The peak in the velocity eigenfunction is at about 25% of the boundary-layer thickness. The hot-wire anemometer is sensitive to mass flux and total temperature. The mass flux eigenfunctions (Fig. 18) show two primary peaks, one that is at 25% of the boundary-layer thickness and a second at the boundary-layer edge that arise from the dominant peaks in the density and velocity eigenfunctions. A less pronounced peak is also observed at 60% of the boundary-layer thickness. The total temperature eigenfunctions (Fig. 19) show a small peak at 10% of the boundary-layer thickness, and a larger peak is located at approximately 75% of the boundary-layer thickness. Because no initial amplitude of the disturbance is specified in LST, the effects of pressure gradient and wall cooling cannot be assessed from Figs. 16–19. However, for a given case it is evident that a hot wire traversed though the boundary layer will give a changing output due to the variations in the mass flux and total temperature eigenfunctions.

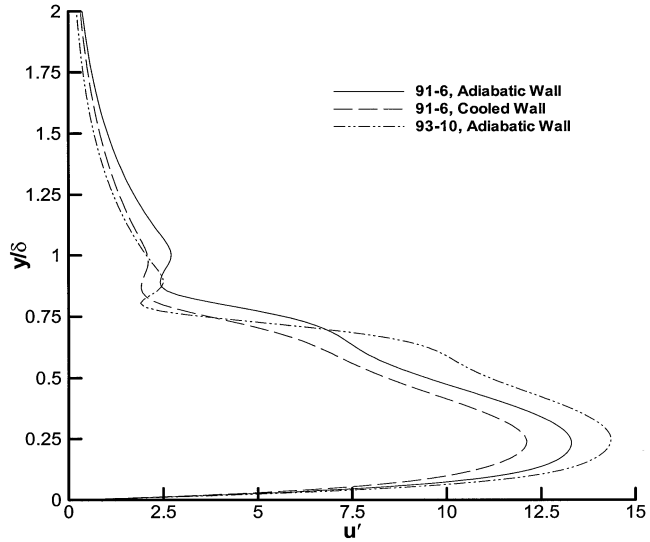

Fig. 17 Velocity eigenfunction for 91–6 and 93–10 models at $x = 13$ in.

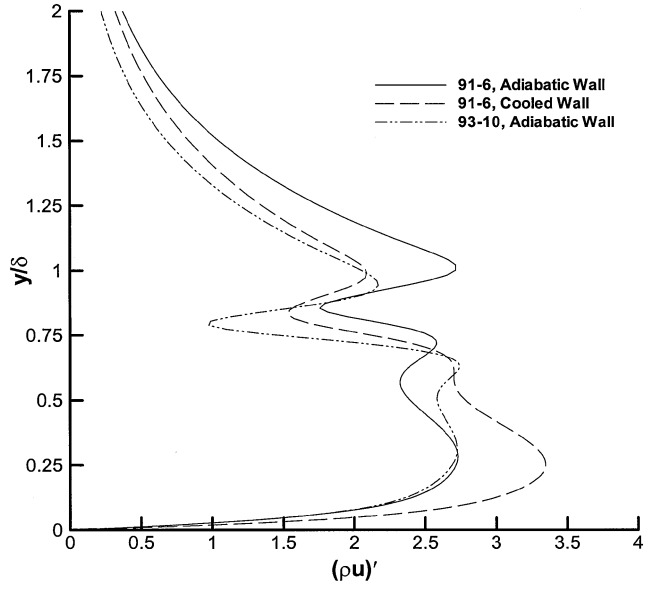

Fig. 18 Mass flux eigenfunction for 91–6 and 93–10 models at $x = 13$ in.

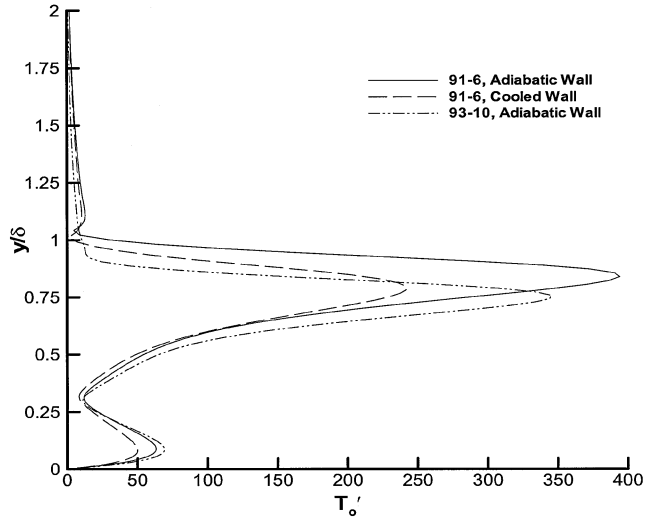

Fig. 19 Total temperature eigenfunction for 91–6 and 93–10 models at $x = 13$ in.

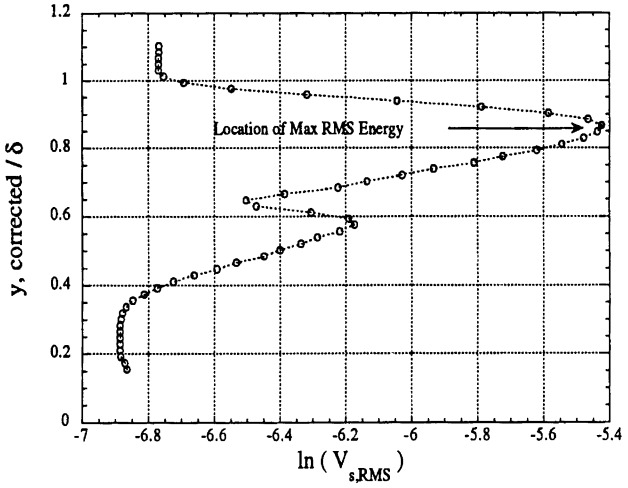

Fig. 20 From Ref. 7, rms hot-wire output, 91–6 adiabatic model.

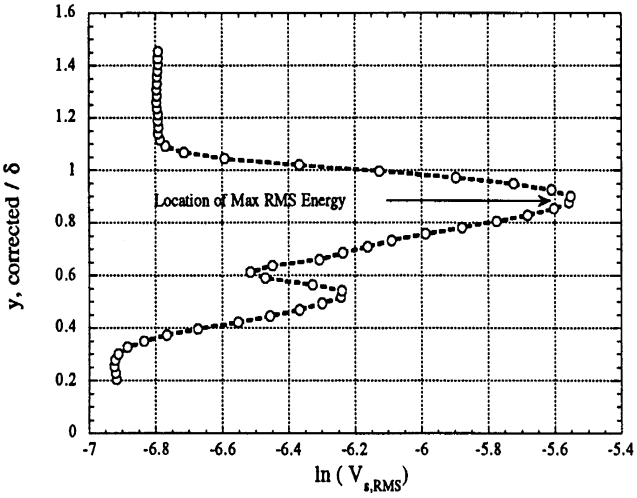

Fig. 21 From Ref. 7, rms hot-wire output, 91–6 cooled model.

Uncalibrated hot-wire measurements on the 91–6 model were obtained with the hot wire operated at a high-overheat mode; thus, the hot wire was most sensitive to mass flux fluctuations. Figures 20 and 21 show the rms anemometer output voltage measured at $x = 9$ in. for the adiabatic and cooled models, respectively. The rms output is a measure of the rms energy in the disturbances. Two peaks are seen in the measured profiles, one at approximately 85% of the boundary-layer thickness and a second one at approximately 55% of the boundary-layer thickness. There are several possible explanations for the double peak seen in the experimental data and the differences between the experimental and LST results. In the experiment, the wire is traversed across the boundary layer, while the wire voltage is kept constant. Because the recovery temperature and wire Reynolds number vary through the boundary layer, the wire's sensitivity to mass flux and total temperature vary through the boundary layer. In Fig. 13, the wire Reynolds number is observed to change significantly over the boundary layer; this change results in a marked change in the CVA output due to its frequency-response characteristics. This complex mixed-mode response of the wire and the variation of the sensitivity coefficients due to the change in the mean flow emphasize the need for calibrated hot-wire measurements in the future. Note the observation of Pruett and Chang[31] that in the experiment the energy of the second mode is distributed over the range of frequencies of the amplified disturbances, whereas the computation is performed only for one frequency, in the present case, the most amplified disturbance.

Conclusions

A computational assessment of two stability experiments performed in the NASA Langley Research Center Nozzle Test Chamber

equipped with the axisymmetric Mach 6 quiet nozzle has been conducted. The computational assessment consists of two parts: Navier–Stokes calculations to simulate the mean flow and linear stability theory to analyze the boundary layer. The objective of this work is to assess the overall quality of the experimental measurements, in particular the CVA-operated hot-wire measurements, and to make recommendations concerning the experimental test procedure. This assessment is of value in the development of future quiet wind-tunnel hypersonic stability experiments.

The computed surface pressures are in very good agreement with the experimental measurements; however, to ascertain the possible effects of model misalignment, it is recommended that surface pressure measurements along a 180-deg out-of-phase ray also be obtained in future experiments. Computed surface temperatures also show overall good agreement with the experiment. The use of a variable wall temperature, fitted to the experimentally measured data, shows that there is neither a significant effect on the mean flow profiles nor on the boundary-layer stability due to the temperature gradient; therefore, it is concluded that the model preheat procedure developed in the previous experiments is satisfactory. The majority of the experimental measurements are uncalibrated hot-wire measurements. In the one case where calibrated hot-wire data are available, the computed and experimental profiles show excellent agreement in the early stages of the transitional flow. In the latter streamwise stations, where nonlinear interactions become important, differences are seen in the profiles. The computed profiles of total temperature show very good agreement with the uncalibrated hot-wire measurements over the outer portion of the boundary layer, when the wire is operated in a low-overheat mode. The computed boundary-layer thickness decreases with both adverse pressure gradient and wall cooling; this is consistent with the experimental observations. However, the comparison of the computed and measured boundary-layer thickness are subjective because the measured data are derived from uncalibrated hot-wire measurements.

The unstable second-mode disturbances are tuned to the boundary-layer thickness; thus, the frequencies of the disturbances increase with adverse pressure gradient and wall cooling. The amplification rates of the unstable disturbances also increase due to adverse pressure gradient and wall cooling. The sensitivity of the hot wire to mass flux and total temperature is examined using the computed wire Reynolds number and eigenfunction profiles. The analyses suggest that, even when operated in the high overheat mode, the sensitivity of the hot wire to total temperature is significant. This is most clearly observed when uncalibrated rms profiles are compared with eigenfunctions of mass flux and total temperature. The eigenfunctions show multiple peaks, whereas the measurements show only two peaks. The variation of the wire Reynolds number across the boundary layer suggests a highly nonlinear response of the hot wire. Thus, whereas uncalibrated hot-wire measurements are useful to characterize the overall features of the flow, calibrated hot-wire measurements are necessary for quantitative flow comparisons with stability theory.

Acknowledgments

The work of the first author was supported by the U.S. Air Force Institute of Technology. The work of the second author was supported, in part, by Air Force Office of Scientific Research Grant F49620-01-1-0105; the Technical Monitor is John D. Schmisseur. The authors are most grateful to the reviewers for their helpful comments on the manuscript. The views and conclusions contained herein are those of the authors and should not be interpreted as necessarily representing the official policies or endorsements, either expressed or implied, of the U.S. Government or the Air Force Office of Scientific Research.

References

[1]Reed, H. L., Kimmel, R., Schneider, S. P., and Arnal, D., "Drag Prediction and Transition in Hypersonic Flow," AIAA Paper 97-1818, June 1997.

[2]Mack, L. M., "Boundary-Layer Stability Theory," *Special Course on Stability and Transition of Laminar Flow*, AGARD-R-709, 1984.

[3]Mack, L. M., "Stability of Axisymmetric Boundary Layers on Sharp Cones at Hypersonic Mach Numbers," AIAA Paper 87-1413, June 1987.

[4]Reshotko, E., "Boundary Layer Instability, Transition, and Control," AIAA Paper 94-0001, Jan. 1994.

[5]Schneider, S. P., "Effects of High Speed Tunnel Noise on Laminar–Turbulent Transition," *Journal of Spacecraft and Rockets*, Vol. 38, No. 3, 2001, pp. 323–333.

[6]Chen, F. -J., Wilkinson, S. P., and Beckwith, I. E., "Görtler Instability and Hypersonic Quiet Nozzle Design," *Journal of Spacecraft and Rockets*, Vol. 30, No. 2, 1993, pp. 170–175.

[7]Lachowicz, J. T., and Chokani, N., "Hypersonic Boundary Layer Stability Experiments in a Quiet Wind Tunnel with Bluntness Effects," NASA CR-198272, Jan. 1996.

[8]Blanchard, A. E., and Selby, G. V., "An Experimental Investigation of Wall-Cooling Effects on Hypersonic Boundary-Layer Stability in a Quiet Wind Tunnel," NASA CR-198287, Feb. 1996.

[9]Sarma, G. R., "Transfer Function Analysis of the Constant Voltage Anemometer," *Review of Scientific Instruments*, Vol. 69, No. 6, 1998, pp. 2385–2391.

[10]Morkovin, M. V., "Fluctuations and Hot Wire Anemometry in Compressible Flow," AGARDograph 24, Nov. 1956.

[11]Lachowicz, J. T., Chokani, N., and Wilkinson, S. P., "Boundary-Layer Stability Measurements in a Hypersonic Quiet Tunnel," *AIAA Journal*, Vol. 34, No. 12, 1996, pp. 2496–2500.

[12]Wilkinson, S. P., "A Review of Hypersonic Boundary Layer Stability Experiments in a Quiet Mach 6 Wind Tunnel," AIAA Paper 97-1819, June 1997.

[13]Beckwith, I. E., "Development of a High Reynolds Number Quiet Tunnel for Transition Research," *AIAA Journal*, Vol. 13, No. 3, 1974, pp. 300–306.

[14]Iyer, V., "Assessment of Meanflow Solutions for Instability Analysis of Transitioning Flows," AIAA Paper 91-1638, June 1991.

[15]Manning, M. L., "Computational Evaluation of Quiet Tunnel Hypersonic Boundary Layer Stability Experiments," M.S. Thesis, Dept. of Mechanical and Aerospace Engineering, North Carolina State Univ., Raleigh, NC, Nov. 2000.

[16]Edwards, J. R., "Nonlinear Relaxation/Quasi-Newton Algorithm for the Compressible Navier–Stokes Equations," *AIAA Journal*, Vol. 31, No. 1, 1993, pp. 57–60.

[17]Edwards, J. R., "A Diagonal Implicit/Nonlinear Multigrid Algorithm for Computing Hypersonic, Chemically-Reacting Viscous Flows," AIAA Paper 94-0762, Jan. 1994.

[18]Edwards, J. R., "A Low-Diffusion Flux-Splitting Scheme for Navier–Stokes Calculations," AIAA Paper 95-1703, June 1995.

[19]Hudson, M. L., Chokani, N., and Candler, G. V., "Linear Stability of Hypersonic Flow in Thermochemical Nonequilibrium," *AIAA Journal*, Vol. 35, No. 6, 1997, pp. 958–964.

[20]Malik, M. R., "Numerical Methods for Hypersonic Boundary-Layer Stability," *Journal of Computational Physics*, Vol. 86, No. 2, 1990, pp. 376–413.

[21]Malik, M. R., "e^{Malik}: A New Spatial Stability Analysis Program for Transition Prediction Using the e^N Method," High Technology Corp., Rept. HTC-9203, Hampton, VA, May 1992.

[22]Chokani,'N., "Nonlinear Spectral Dynamics of Hypersonic Laminar Boundary Layer Flow," *Physics of Fluids*, Vol. 12, No. 12, 1999, pp. 3846–3851.

[23]Chokani, N., "Wavelet Analysis of a Hypersonic Laminar Boundary Layer Flow," AIAA Paper 2000-0535, Jan. 2000.

[24]Doggett, G. P., Chokani, N., and Wilkinson, S. P., "Effects of Angle of Attack on Hypersonic Boundary Layer Stability in a Quiet Wind Tunnel," *AIAA Journal*, Vol. 35, No. 3, 1997, pp. 464–470.

[25]Reimann, C. A., Chokani, N., and Sarma, G. R., "Calibrated Measurements using a CVA-Operated Hot-Wire in a Hypersonic Laminar Boundary Layer," AIAA Paper 2002-0152, Jan. 2002.

[26]Comte-Bellot, G., and Sarma, G. R., "Constant Voltage Anemometer Practice in Supersonic Flows," *AIAA Journal*, Vol. 39, No. 2, 2001, pp. 261–270.

[27]Sarma, G. R., Comte-Bellot, G., and Faure, T. M., "Software Corrected Hot Wire Thermal Lag for the Constant Voltage Anemometer Featuring a Constant Bandwidth at the Selected Compensation Setting," *Review of Scientific Instruments*, Vol. 69, No. 9, 1998, pp. 3223–3231.

[28]Stetson, K. F., Thompson, E. R., Donaldson, J. C., and Siler, L. G., "Laminar Boundary Layer Stability Experiments on a Cone at Mach 8, Part 1: Sharp Cone," AIAA Paper 83-1761, July 1983.

[29]Kimmel, R. L., Demetriades, A., and Donaldson, J. C., "Space-Time Correlation Measurements in a Hypersonic Transitional Boundary Layer," *AIAA Journal*, Vol. 34, No. 12, 1996, pp. 2484–2489.

[30]Kimmel, R. L., and Poggie, J., "Effect of Total Temperature on Boundary Layer Stability at Mach 6," *AIAA Journal*, Vol. 38, No. 9, 2000, pp. 1754–1755.

[31]Pruett, C. D., and Chang, C.-L., "Direct Numerical Simulation of Hypersonic Boundary-Layer Flow on a Flared Cone," *Theoretical and Computational Fluid Dynamics*, Vol. 11, No. 1, 1998, pp. 49–67.

T. C. Lin
Associate Editor